BMC Cancer

RESEARCH

Open Access

Interplay of disulfidptosis and the tumor microenvironment across cancers: implications for prognosis and therapeutic responses

Shengshan Xu[1,2,3*†], Zizhou Chen[1,2†], Xiguang Chen[4†], Hongyu Chu[5], Xufeng Huang[6], Chunyu Chen[7], Hejie Liu[3], Yuting Qu[8,9] and Zhuming Lu[3*]

Abstract

The recent elucidation of disulfidptosis, a unique form of cell death, has opened new paths for the development of targeted cancer therapies. However, a thorough examination of disulfidptosis-related genes (DRGs) across various cancer types has been lacking. Our extensive analysis of DRGs through genomic, transcriptional, and immune profiling has yielded substantial insights. Utilizing The Cancer Genome Atlas (TCGA), we have identified key changes in gene expression, including alterations in copy number and DNA methylation, and evaluated their impact on cancer prognosis. We constructed a disulfidptosis-related signature (DFRS) using LASSO regression and multivariate Cox regression analysis, which demonstrated a strong prognostic connection across diverse cancer types. The DFRS score is linked with poorer clinical outcomes, reflects the immune characteristics of the tumor microenvironment (TME), and predicts responsiveness to immunotherapy and other treatments. Notably, the DFRS score interacts with critical oncogenic pathways, highlighting the potential benefits of targeting disulfidptosis in cancer treatment. Our findings underscore the critical influence of disulfidptosis on cancer prognosis and therapeutic response, offering meaningful clinical insights.

Keywords Pan-cancer, Disulfidptosis, Prognosis, Immunotherapy, Tumor microenvironment

†Shengshan Xu, Zizhou Chen and Xiguang Chen contributed equally to this work and share the first authorship.

*Correspondence:
Shengshan Xu
xushengshan97@163.com
Zhuming Lu
lzm219@jnu.edu.cn
[1] Scientific Research Center, The Seventh Affiliated Hospital, Sun Yat-Sen University, Shenzhen, Guangdong, China
[2] Department of Thoracic Surgery, The Seventh Affiliated Hospital, Sun Yat-Sen University, Shenzhen, Guangdong, China
[3] Department of Thoracic Surgery, Jiangmen Central Hospital, Jiangmen, Guangdong, China
[4] Department of Medical Oncology, The First Affiliated Hospital of University of South China, Hengyang, Hunan, China
[5] Department of Gastrointestinal, Colorectal and Anal Surgery, China-Japan Union Hospital of Jilin University, Changchun, Jilin, China
[6] University of Debrecen, Debrecen, Hungary
[7] Department of Infectious Disease, Jiangmen Central Hospital, Jiangmen, Guangdong, China
[8] Zunyi Medical University, Zunyi, Guizhou, China
[9] Department of Breast Surgery, Guizhou Provincial People's Hospital, Guiyang, Guizhou, China

Introduction

The American Cancer Society underscores cancer as a major global health issue, projecting that by 2023, there will be approximately 1,958,310 new cases and 609,820 deaths due to cancer in the United States [1]. Given cancer's complex nature, understanding its molecular underpinnings is crucial for advancing early detection and developing more effective therapeutic strategies [2].

Recent studies have compellingly linked disulfide metabolism to the progression of cancer. This pathway, integral to cellular redox processes, involves critical formation and breakdown of disulfide bonds. Notably, cancer cells often experience oxidative stress, leading to significant changes in disulfide metabolism that influence cell proliferation and survival [3]. Furthermore, disulfide metabolism in cancer is intricately linked with key biological processes such as drug resistance, metastasis, and immune evasion [4, 5].

Disulfidptosis represents a novel form of cell death, distinguished from traditional programmed cell death pathways. It is marked by a mismatch in cysteine intake and NADPH availability, leading to abnormal disulfide bonds within actin cytoskeletal proteins. This imbalance prompts excessive disulfide build-up, causing stress and subsequent disruption of the actin structure, ultimately leading to cell death [6, 7]. Given its unique mechanisms, disulfidptosis presents a promising avenue for cancer therapy. Emerging evidence reveals that disulfidptosis is not merely a metabolic accident but involves intricate molecular cross-talk. For instance, SLC7 A11-mediated cystine uptake initiates disulfidptosis under glucose deprivation, while recent studies demonstrate that endoplasmic reticulum (ER) stress acts as a protective feedback mechanism to counteract disulfidptosis by maintaining redox homeostasis [8]. Pharmacological inhibition of ER stress synergizes with glucose transporter inhibitors to amplify cytoskeletal disulfide crosslinking, suggesting a dynamic interplay between organelle-specific stress responses and disulfidptotic susceptibility.

Given its unique mechanisms, disulfidptosis presents a promising avenue for cancer therapy. Intriguingly, its implications extend beyond oncology. Aberrant SLC7 A11 expression exacerbates glutathione depletion in Parkinson's disease models, accelerating neuronal loss [9]. While direct evidence linking disulfidptosis to neurodegeneration remains scarce, the shared reliance on NADPH buffering between cancer and neuronal systems suggests potential mechanistic overlaps. Future studies should explore whether disulfidptosis contributes to pathological protein aggregation or axonal degeneration in conditions like Alzheimer's disease. Nevertheless, research into the genetic variations and clinical relevance of disulfidptosis-related genes (DRGs) in different cancers remains limited. To fill this gap, we conducted a detailed multi-omics analysis of 23 DRGs across various cancers.

Our study incorporated evaluations of somatic copy number alterations (SCNA), single nucleotide variations (SNV), and DNA methylation patterns. Utilizing LASSO and multivariate Cox analyses, we developed a disulfidptosis-related signature (DFRS) using pan-cancer data. This model seeks to refine prognostic predictions for individual patients. We observed that the DFRS score is linked with malignant pathways, patient outcomes, the tumor microenvironment (TME), and responses to immunotherapy, emphasizing the potential therapeutic implications of disulfidptosis.

Materials and Methods

Patients and datasets

Our research utilized pan-cancer data from four major platforms: the Molecular Taxonomy of Breast Cancer International Consortium (METABRIC, http://www.cbioportal.org), The Cancer Genome Atlas (TCGA, http://cancergenome.nih.gov/), the International Cancer Genome Consortium (ICGC, https://dcc.icgc.org/), and the Chinese Glioma Genome Atlas (CGGA, http://www.cgga.org.cn). A detailed list of the 32 cancer types, abbreviations, and sample sizes is provided in Supplementary Table 1.

We gathered datasets containing gene expression data and corresponding clinical information from the Gene Expression Omnibus database (GEO, https://www.ncbi.nlm.nih.gov/geo/), including GSE103479, GSE84437, GSE72094, GSE53922, GSE32894, GSE13507, GSE30219, GSE17538, and GSE17118. To evaluate the responses to cisplatin and bevacizumab treatment in a neoadjuvant context, the GSE103668 dataset was used. Data pertaining to immunotherapy responses were derived from GSE91061, phs000452, and PRJEB23709 [10], as well as two clinical in-house cohorts, with an overview provided in Supplementary Table 2. The two clinical in-house cohorts respectively include information on lung adenocarcinoma and melanoma tissues from patients who received immunotherapy, and all patients provided informed consent.

Analysis of mRNA differential expression

We utilized the "limma" package [11] to assess expression differences in DRGs between tumor and adjacent normal tissues across 20 cancer types. Significant genes were identified through adjusted P values less than 0.05 and visualized in a bubble chart. To explore the relationship between DRG expression and patient survival, we applied Cox regression analysis to compare survival metrics across these groups.

Analysis of Single Nucleotide Variations (SNVs)

SNV data were extracted from the TCGA database. For the purpose of determining SNV percentages, we excluded silent, intron, IGR, 3'UTR, 5'UTR, 3'flank, and 5'flank sequences. Mutation frequencies were calculated by the ratio of mutated cases to the total number of cancer cases. The SNV analysis was depicted using an oncoplot generated by the "maftools" package in R.

Somatic Copy Number Alteration (SCNA) analysis

We analyzed both heterozygous and homozygous amplifications and deletions to evaluate gene-specific copy number variations. Variations present in more than 5% of samples were classified as high-frequency SCNAs. We then investigated the association between SCNAs and gene expression by calculating Pearson's correlations for each gene.

Analysis of DNA methylation patterns

DNA methylation data for 33 cancer types were retrieved from the TCGA database. We used the Wilcoxon signed-rank test to identify differences in methylation levels of DRGs between tumor and corresponding normal tissues. Significant changes in methylation were determined using a threshold P value of 0.05, identifying either hypo- or hypermethylation. Additionally, we explored the impact of promoter methylation on gene expression using Spearman's correlation, applying the same significance criteria.

Constructing a Disulfidptosis-Related Signature (DFRS)

From the TCGA datasets, 70% of the samples (6484 out of 9264) were randomly selected for the training set, with the remaining 30% (2780 out of 9264) used as the testing set. We utilized the LASSO algorithm and multivariate Cox analyses to develop the DFRS, aiming to simplify the model and minimize overfitting. The DFRS score was computed using the following formula: $\text{DFRS Score} = [(0.089 \times \textit{Expression value of SLC7A11}) + (0.2 \times \textit{Expression value of NDUFS1}) + [(-0.374) \times \textit{Expression value of NDUFA11}] + [(-0.106) \times \textit{Expression value of NUBPL}] + (0.1 \times \textit{Expression value of NCKAP1}) + (0.154 \times \textit{Expression value of RPN1}) + (0.2 \times \textit{Expression value of ACTN4}) + (0.386 \times \textit{Expression value of ACTB}) + [(-0.073) \times \textit{Expression value of CD2AP}] + (0.039 \times \textit{Expression value of FLNA}) + [(-0.227) \times \textit{Expression value of FLNB}] + (0.185 \times \textit{Expression value of INF2}) + [(-0.14) \times \textit{Expression value of IQGAP1}] + (0.208 \times \textit{Expression value of MYL6})]$. Samples were then classified into high or low DFRS groups based on the median score. The predictive capability of the DFRS was evaluated using external datasets.

Evaluation of the DFRS score's prognostic value

The prognostic significance of the DFRS score was determined using Cox proportional hazards regression analyses, with results visualized through the "ggforest" function. The Kaplan–Meier method was applied to evaluate the significance of differences in survival rates across various cancers, considering a P value of less than 0.05 as statistically significant.

Exploration of the value of the DFRS in clinical utility

To enhance the real-world applicability of the DFRS, we constructed a nomogram that includes patient age, cancer type, and DFRS score to forecast the overall survival (OS) at 1, 3, 5, and 10 years. We also verified the accuracy of the nomogram using a calibration curve to evaluate its precision in predicting survival outcomes.

Assessment of biological processes using the Z score

We applied the z-score technique to quantify the activity of specific biological pathways by measuring the expression levels of associated genes [12]. Gene sets, which encompass genes related to angiogenesis [13], epithelial to mesenchymal transition (EMT), and the cell cycle [14], were processed using the z-score method [15]. We then employed single-sample gene set enrichment analysis (ssGSEA) to calculate enrichment scores for gene sets associated with disulfidptosis. Based on these scores, samples were categorized into higher and lower 50% groups, followed by a comprehensive gene set enrichment analysis (GSEA) [16].

Correlation of DFRS score with immune characteristics across cancers

To explore the influence of disulfidptosis on the tumor microenvironment, we calculated Pearson correlation coefficients to assess the relationship between the DFRS score and various immune-related scores, including immune, stromal, and ESTIMATE scores. Furthermore, we utilized the CIBERSORT algorithm to analyze immune cell infiltration within the TCGA pan-cancer datasets [17].

Processing for RNA sequencing

RNA sequencing was performed on 32 lung adenocarcinoma (LUAD) and 13 melanoma tissue specimens from two in-house cohorts (Supplementary Table 3–4). Total RNA was extracted from these tissue samples using TRIzol reagent (Sigma–Aldrich, CA, USA). The RNA purity was assessed using a NanoPhotometer (IMPLEN, CA, USA), followed by the RNA Nano 6000 Assay Kit on a Bioanalyzer 2100 system (Agilent Technologies, CA, USA). Each specimen had 1 μg of RNA as input for sample preparation. Sequencing libraries were then constructed using the NEBNext® UltraTM RNA Library Prep Kit, designed for Illumina® systems (NEB, USA).

Drug responsiveness related to DFRS score

To evaluate the clinical impact of DFRS, we investigated their association with 141 clinically actionable genes (CAGs), which include 121 genes targeted by therapies and 20 genes linked to immunotherapy responses across different cancers [18, 19]. To establish the relationship between small-molecule drugs and the DFRS score, we sourced area under the dose–response curve (AUC) data for drugs tested on pan-cancer cell lines from the Genomics of Drug Sensitivity in Cancer (GDSC) database (https://www.cancerrxgene.org/downloads) [20]. We then determined the correlations between the AUC values and DFRS scores. Only correlations with coefficients greater than 0.1 and a *P* value below 0.05 were deemed significant.

Cell Culture

We cultured lung adenocarcinoma cell lines, specifically A549 and PC-9, alongside BEAS-2B cells originating from normal human alveolar epithelial tissue, acquired from the American Type Culture Collection (ATCC) in Rockville, MD, USA. These cells were grown in Dulbecco's Modified Eagle's Medium (DMEM) enriched with 10% fetal bovine serum from Gibco (Waltham, MA, USA), and maintained at 37 °C in a 5% CO2 atmosphere with optimal humidity. We conducted migration and colony formation assays on the A549 cell line.

RNA interference and transfection

For gene silencing, we used small interfering RNAs (siRNAs) targeting NCKAP1 and ACTN4, obtained from Tsingke Bio Technology Co., Ltd. (Beijing, China). Two distinct siRNA sequences were designed for each target gene: si-NCKAP1-1: 5'-CAUCCUAUCUUAUCGACAA-3' and si-NCKAP1-2: 5'-CAGACGACUUUAUAGAUAA-3', si-ACTN4-1: 5'- GCCACACUAUCGGACAUCAAA-3', and si-ACTN4-2: 5'- CAUCGCUUCCUUCAAGGUCUU-3'. Transfections were performed on A549 cells using 50 nmol/L of these siRNAs with Lipofectamine 2000 (ThermoFisher, Massachusetts, USA), and the knockdown efficiency was verified by RT-qPCR.

RT-qPCR

RNA was extracted from the cells using Trizol reagent (Vazyme, Nanjing, China, R411-01) and reverse transcribed using HiScript III RT SuperMix (Vazyme, China, R323). RT-qPCR was performed with the Universal SYBR Green Fast qPCR Mix (ABclonal, Hong Kong, China, RK21203), using the $2^{(-\Delta\Delta Ct)}$ method for quantification of gene expression, with GADPH serving as the internal control. Primer details are listed in Supplementary Table 5.

Clone formation assays

Post-transfection, cells were seeded in 6-well plates. Following a two-week incubation, colonies were fixed with 4% paraformaldehyde for 30 min and stained with 0.1% crystal violet for another 30 min. Colony images were captured and analyzed using high-resolution ImageJ software.

Cell migration assay

The migratory ability of LUAD cells was assessed using a transwell setup (Corning 3422, 8 μm pore size) without Matrigel. Cells were seeded in serum-free medium in the upper chamber, and the lower chamber was filled with medium containing 10% FBS. After 24 h at 37 °C, cells were fixed and non-migratory cells were removed. The migrated cells were stained with crystal violet, air-dried, and imaged.

Statistical analysis

Data were expressed as mean ± standard deviation (SD). Statistical analyses were performed using ggplot2 in R and GraphPad Prism 8, with a significance threshold set at $P < 0.05$. Each experiment was replicated three times to ensure consistency and reproducibility.

Results

Genomic variations of DRGs in different cancers

To elucidate the dysregulation of DRGs, we analyzed comprehensive genomic datasets that included gene expression, SNVs, SCNAs, and DNA methylation across multiple cancer types. We focused on DRG SNP datasets to determine the prevalence and types of mutations. Our analysis showed particularly high mutation rates in skin cutaneous melanoma (SKCM), uterine corpus endometrioid carcinoma (UCEC), colon adenocarcinoma (COAD), and bladder urothelial carcinoma (BLCA), with a notable mutation rate of 72.61% (1776 out of 2446 tumors) highlighted in Figure S1A. Predominantly, missense mutations were observed, and the genes most frequently mutated were FLNA, FLNB, MYH9, TLN1, MYH10, IQGAP1, LRPPRC, ACTN4, NCKAP1, and INF2, showing mutation rates of 17%, 15%, 14%, 12%, 11%, 8%, 7%, 7%, 6%, and 5%, respectively, as detailed in Figure S1B.

SCNAs are widespread in cancers and significantly impact tumor development. We closely examined SCNA occurrences in DRGs across various cancers. The analysis revealed a varied prevalence of SCNAs, with kidney renal papillary cell carcinoma (KIRP), uveal melanoma (UVM), and lymphoid neoplasm diffuse large B-cell lymphoma (DLBC) generally showing a lower frequency of SCNA in most DRGs, as depicted in Fig. 1A. The SCNA profiles of DRGs varied widely; for example, genes such

as RPN1, ACTB, and DSTN typically showed more frequent copy number gains than losses, whereas SCL7 A11 and PDLIM1 displayed the opposite pattern.

Aberrant expression and prognostic implications of DRGs across cancers

We undertook a comparative analysis of DRG expression between tumor samples and adjacent normal tissues to identify variations in expression profiles. This investigation revealed that every DRG showed differential expression in at least one cancer type, displaying unique expression patterns across different cancers. For instance, SLC7 A11 was significantly overexpressed in 15 cancer types, while TLN1 predominantly showed under-expression (Fig. 1B). Subsequently, we assessed the prognostic impact of DRGs utilizing the Cox proportional hazards model, determining hazard ratios (HRs) and p-values for each gene. DRGs with HRs greater than 1 and p-values below 0.05 were considered risk factors, whereas those with HRs less than 1 and p-values below 0.05 were deemed protective. The results suggested that each DRG correlated with survival outcomes in at least one type of cancer (Fig. 1C). Further, we explored the effect of somatic copy number alterations (SCNAs) on DRG expression, revealing a strong association between SCNAs and gene expression changes across many tumors (Fig. 1D). In addition to SCNAs, promoter methylation is another pivotal factor modulating gene expression. Notably, aberrant DNA methylation within the promoter region has been linked to the onset of tumors [21]. We proceeded to examine the methylation levels of DRG promoters across various cancers. Our analysis revealed intricate methylation patterns for DRGs in pan-cancer studies, with a predominant trend toward hypermethylation (Fig. 1E). While the methylation patterns for DRGs varied, a pronounced correlation was evident between methylation status and DRG expression levels (Fig. 1F), highlighting the importance of SCNAs and promoter methylation in modulating DRG expression across cancers, suggesting further areas for regulatory mechanism exploration.

Pan-cancer identification of a 14-gene DFRS

Delving into the role of disulfidptosis in cancer progression, we identified a 14-gene DFRS suitable for pan-cancer application. Starting with 23 candidate DRGs, we applied LASSO regression within the TCGA training cohort to refine the selection (Fig. 2A). Subsequent multivariate Cox regression analysis identified 14 prognostically significant genes—ACTB, ACTN4, CD2 AP, FLNA, FLNB, INF2, IQGAP1, MYL6, NCKAP1, NDUFS1, NUBPL, RPN1, NDUFA11, and SLC7 A11. These genes formed the basis of the DFRS. Further analyses revealed similarities in expression trends among some of these genes (Fig. 2B), and the hazard ratios for each were evaluated to assess their prognostic relevance (Fig. 2C).

Landscape of DFRS in multiple cancers

The DFRS score demonstrated distinct tissue-specific patterns. Predominantly high DFRS scores were observed in tumors originating from the brain and gastrointestinal tract. Conversely, low scores were commonly seen in tumors from specific endocrine glands such as adrenocortical carcinoma (ACC), prostate carcinoma (PRAD), thyroid carcinoma (THCA), pheochromocytoma and paraganglioma (PCPG), and breast invasive carcinoma (BRCA) (Fig. 3A). Interestingly, despite originating from similar tissues, brain lower-grade glioma (LGG) displayed significantly lower DFRS scores compared to glioblastoma multiforme (GBM). Within the TCGA training set, patients were classified into high or low DFRS groups based on median scores. A high DFRS score correlated with poorer outcomes across multiple survival metrics including overall survival (OS), disease-specific survival (DSS), and progression-free interval (PFI) (Fig. 3B). Validation of the signature's prognostic significance was also confirmed in both training and testing cohorts of the

(See figure on next page.)

Fig. 1 Dysregulation of disulfidptosis-related genes (DRGs). **A** Graphical representation of the frequency of somatic copy number variations for DRGs in diverse cancer forms. Each bar represents a different cancer type, and the horizontal axis quantifies the frequency of observed SCNVs. **B** This heatmap illustrates the differential expression of DRGs in various tumor tissues compared to normal counterparts. The expression levels are log2-transformed fold changes (log2 FC), with red indicating upregulation and green indicating downregulation. The size of each circle within the heatmap cells reflects the statistical significance (**C**) A summary of the relationship between the expression of DRGs and survival in various cancers. Red indicates genes whose upregulation is correlated with poorer survival, and blue indicates genes correlated with better survival. Only results with $p < 0.05$ are presented. **D** This heatmap presents the relationship between somatic copy number changes and the expression levels of DRGs, analyzed using Spearman's correlation coefficient. The size of each circle within the heatmap cells reflects the statistical significance. (E) Heatmap showing the methylation variations in DRGs across cancer types; hypermethylated and hypomethylated genes are indicated in red and blue, respectively (Wilcoxon signed-rank test). The size of each circle within the heatmap cells reflects the statistical significance. **F** Pearson correlation analysis of DRG expression and promoter methylation. Red signifies positive associations, and blue denotes negative associations

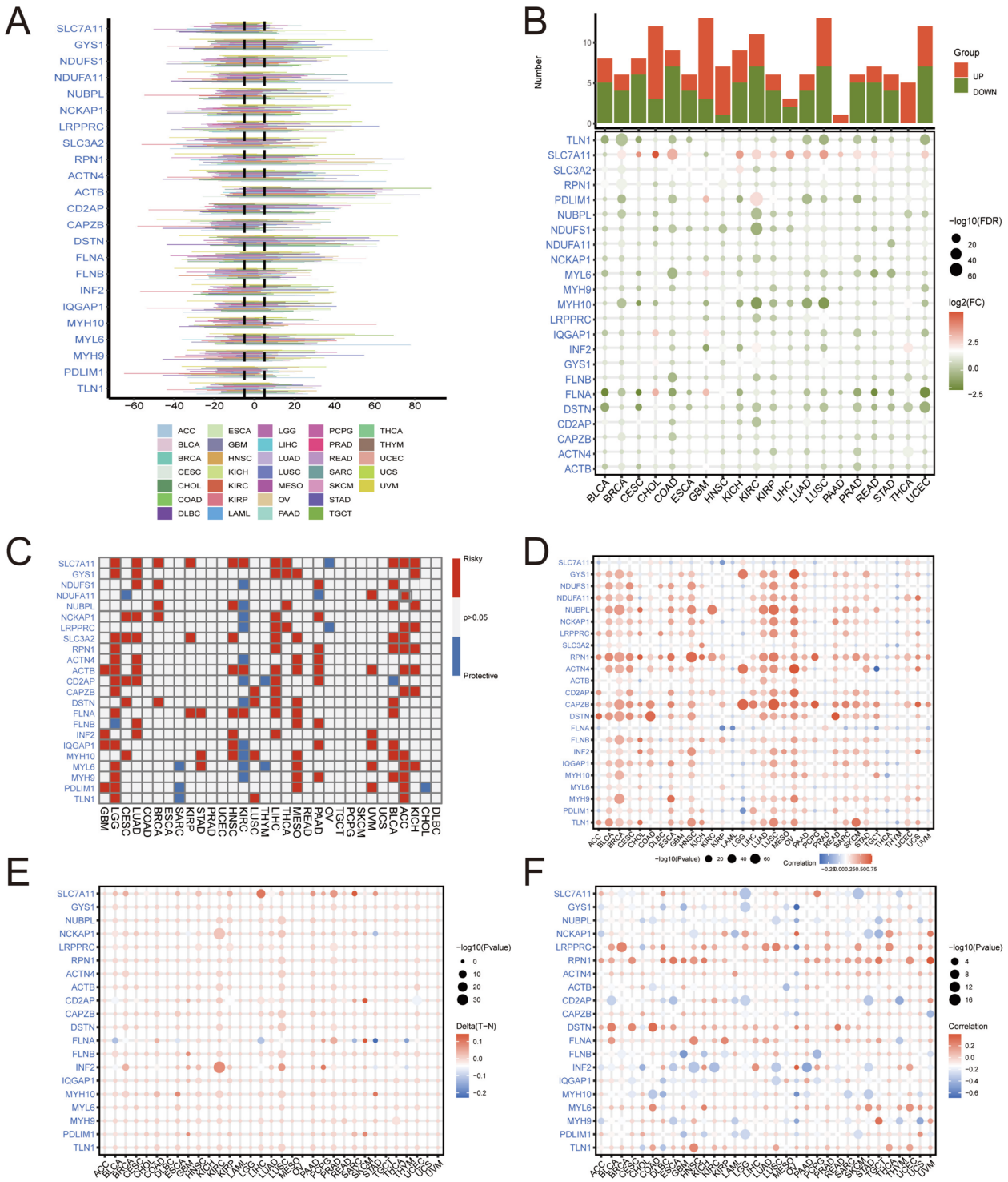

Fig. 1 (See legend on previous page.)

TCGA, where high DFRS scores consistently indicated worse clinical outcomes (Fig. 3C, D). Kaplan–Meier survival plots for OS, DSS, and PFI across various cancer types in the training cohort are depicted in Figs. 4, S3, and S4. The results indicate that a high DFRS score is associated with poorer prognosis in terms of OS across multiple cancer types, including head and neck squamous cell carcinoma (HNSC), kidney renal clear

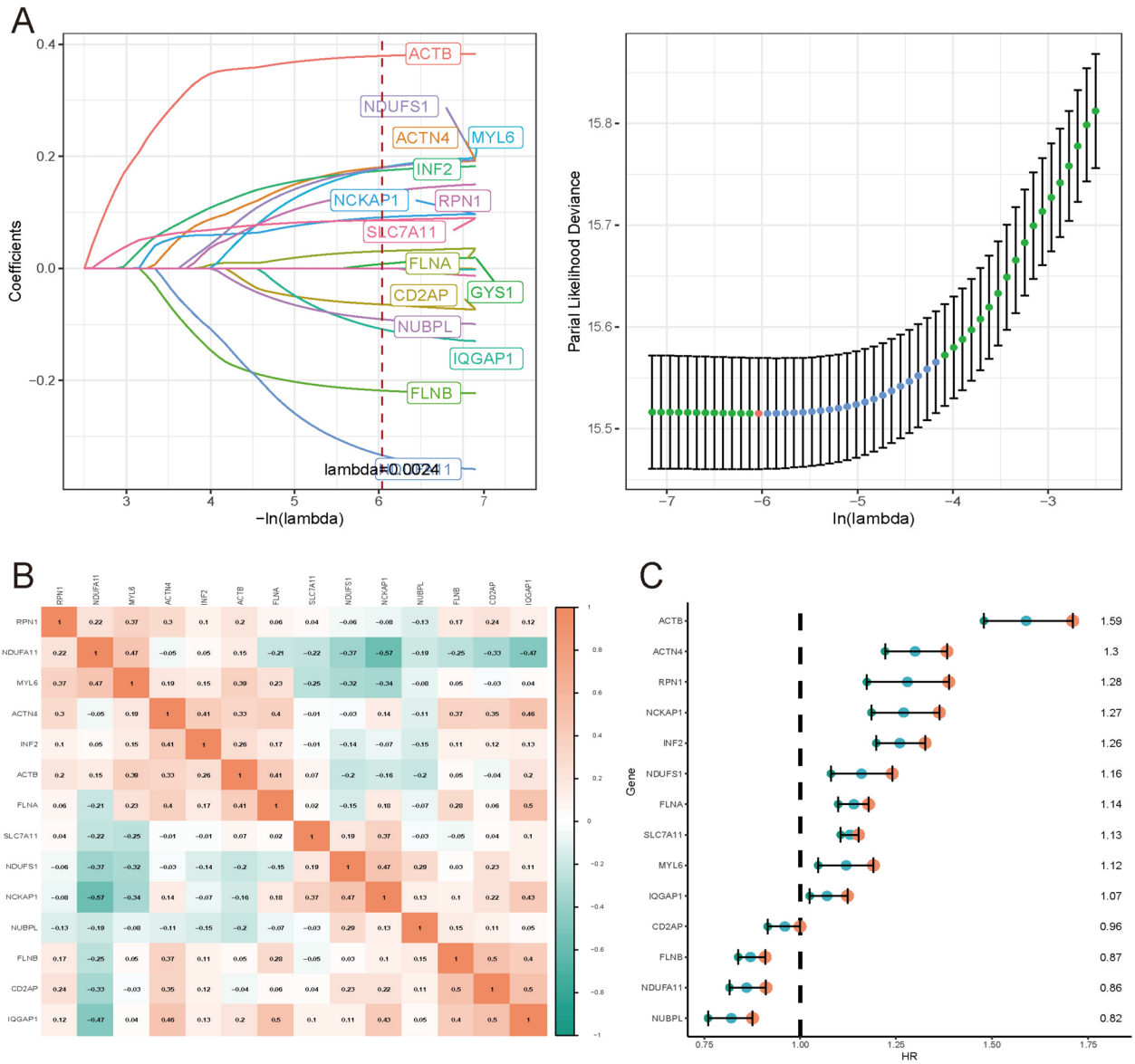

Fig. 2 Identification of a disulfidptosis-related signature (DFRS) across cancers. **A** This graph illustrates the confidence intervals and the trajectory of the regularization parameter lambda for differentially expressed genes involved in disulfidptosis. The x-axis represents the value of lambda. Each line represents a gene, showing how its importance in the model varies as lambda changes. **B** The association between the DFRS core genes is visualized using TCGA pan-cancer information. A darker shade implies a more robust association. **C** This forest plot displays the hazard ratios for each DRG, quantifying their impact on survival in cancer patients. The x-axis represents the hazard ratio, with markers placed at the point estimate for each gene and horizontal lines showing the 95% confidence intervals. Genes to the right of the vertical line at 1.0 are associated with increased risk (poorer survival), whereas genes to the left are associated with decreased risk (better survival)

cell carcinoma (KIRC), KIRP, liver hepatocellular carcinoma (LIHC), lung adenocarcinoma (LUAD), pancreatic adenocarcinoma (PAAD), THCA, and UCEC. For DSS, a similar trend is observed in BRCA, HNSC, KIRC, KIRP, LIHC, LUAD, THCA, and UCEC, where a high DFRS correlates with worse outcomes. Furthermore, in the context of PFI, high DFRS scores are linked to unfavorable prognoses in HNSC, KIRP, LUAD, THCA, and UCEC.

Univariate Cox analysis across various cancer types showed that the DFRS score served as a significant prognostic indicator (Fig. 3E). The pan-cancer univariate analysis yielded the following results. (1) Within the training cohort, the DFRS score acted as a risk

determinant in cancers such as LUAD (HR = 1.714), BLCA (HR = 1.225), KIRP (HR = 1.977), cervical squamous cell carcinoma and endocervical adenocarcinoma (CESC, HR = 1.517), LIHC (HR = 1.552), UCEC (HR = 1.562), KIRC (HR = 1.776), HNSC (HR = 1.386), LGG (HR = 1.789), and UVM (HR = 2.967). (2) In the testing set, the DFRS score emerged as a notable risk factor in cancers such as LUAD (HR = 1.390), GBM (HR = 2.251), lung squamous cell carcinoma (LUSC, HR = 1.447), UCEC (HR = 2.230), HNSC (HR = 1.647), LGG (HR = 3.589), and UVM (HR = 3.793). These findings revealed that the DFRS score is a potential prognostic biomarker for five cancer types, namely, LUAD, UCEC, HNSC, LGG, and UVM. Receiver operating characteristic (ROC) curve analysis revealed area under the curve values of 0.68, 0.7, and 0.69 for 1-, 3-, and 5-year OS in the training set (Figure S5A); the area under the curve values for the testing set were 0.68, 0.7, and 0.68 (Figure S5B), signifying that the DFRS possessed moderate predictive precision. We extended its application to several external validation groups, and the findings similarly showed that a high DFRS score corresponded to a worse prognosis (Figure S6). Interestingly, although there was no notable disparity between the high and low DFRS score groups in the TCGA-BRCA dataset, the DFRS score had a good predictive value in HER-2-positive breast cancer and triple-negative breast cancer subgroups in the METABRIC dataset. In summary, these results suggest that the DFRS score may have a predictive value in certain cancer types, particularly where significant associations with prognosis were observed.

Developing a nomogram including the DFRS score for predicting patient survival across cancer types

To enhance the practical application of the DFRS score in clinical prognosis, we created a detailed nomogram that combines the DFRS score with other clinical factors such as patient age and specific cancer types (Fig. 5A). The calibration curves for 3-year and 5-year overall survival (OS), shown in Fig. 5B, closely match the ideal model, indicating an accurate predictive performance by the nomogram compared to actual survival outcomes.

Correlation of DFRS score with tumor malignancy features

The transformation of normal cells to a malignant state involves changes like increased proliferation, active epithelial-mesenchymal transition (EMT), and enhanced angiogenesis, reflecting aggressive tumor traits. Using z-score normalized analyses across the TCGA pan-cancer dataset, our findings demonstrated positive correlations between the DFRS z-score and EMT z-score (R = 0.3, $p < 2.2e-16$), as well as cell cycle z-score (R = 0.13, $p < 2.2e-16$) (Fig. 6B-C). Moreover, Cancer-type specific analysis revealed heterogeneous DFRS-EMT associations across 32 malignancies (Fig. 6D). Although statistically significant ($p = 1.4e-12$), the DFRS-angiogenesis correlation was negligible (R = 0.07) (Fig. 6A). Additionally, we explored the connection between the DFRS score and GSVA scores of pathways known to facilitate tumor growth. Our analysis showed significant links with several critical pathways, notably the IL6-JAK-STAT3 and WNT beta-catenin signaling pathways, which were particularly active in tumors with high DFRS scores (Fig. 6E). This association underscores that increased disulfidptosis within the tumor microenvironment aligns with more aggressive tumor characteristics.

Interaction of DFRS score with the tumor microenvironment

Tumor immunity is crucial for influencing tumor progression and determining patient outcomes [22]. Examining the impact of disulfidptosis on tumor immunity, we utilized the ESTIMATE algorithm to derive immune scores, stromal scores, and overall ESTIMATE scores across the TCGA pan-cancer dataset [23]. Multivariate linear regression, adjusted for cancer type, revealed significant correlations between the DFRS score and these

(See figure on next page.)

Fig. 3 Prognostic performance of the 14-gene disulfidptosis-related signature (DFRS). **A** This plot visualizes the distribution of DFRS scores among the study population, arranged sequentially from the highest to the lowest. The x-axis represents individual patients, organized in ascending order of their DFRS scores, while the y-axis quantifies the DFRS scores. **B** This bubble chart graphically represents the results of Cox proportional hazards analysis, examining the impact of DFRS scores on survival across different cancer types. Different bubble colors correspond to different types of cancer and the size of the bubble indicating the statistical significance of the association. **C** Kaplan–Meier graphs highlighting the link between the DFRS score and indicators such as overall survival (OS), progression-free interval (PFI), and disease-specific survival (DSS) in the TCGA pan-cancer training set ($n = 6484$) (log-rank test, $p < 0.05$). The curves segregate patients based on median DFRS score into high and low groups. **D** Kaplan–Meier analysis displays the relationship between the DFRS score and OS, PFI, and DSS for patients in the TCGA pan-cancer testing set ($n = 2780$) (log-rank test, $p < 0.05$). Blue represents high DFRS score, and yellow represents low DFRS score. **E** Forest plots depicting univariate Cox regression outcomes in the training and test sets. Each plot evaluates the hazard ratios for DFRS in predicting survival outcomes, with points representing the hazard ratios and horizontal lines denoting 95% confidence intervals

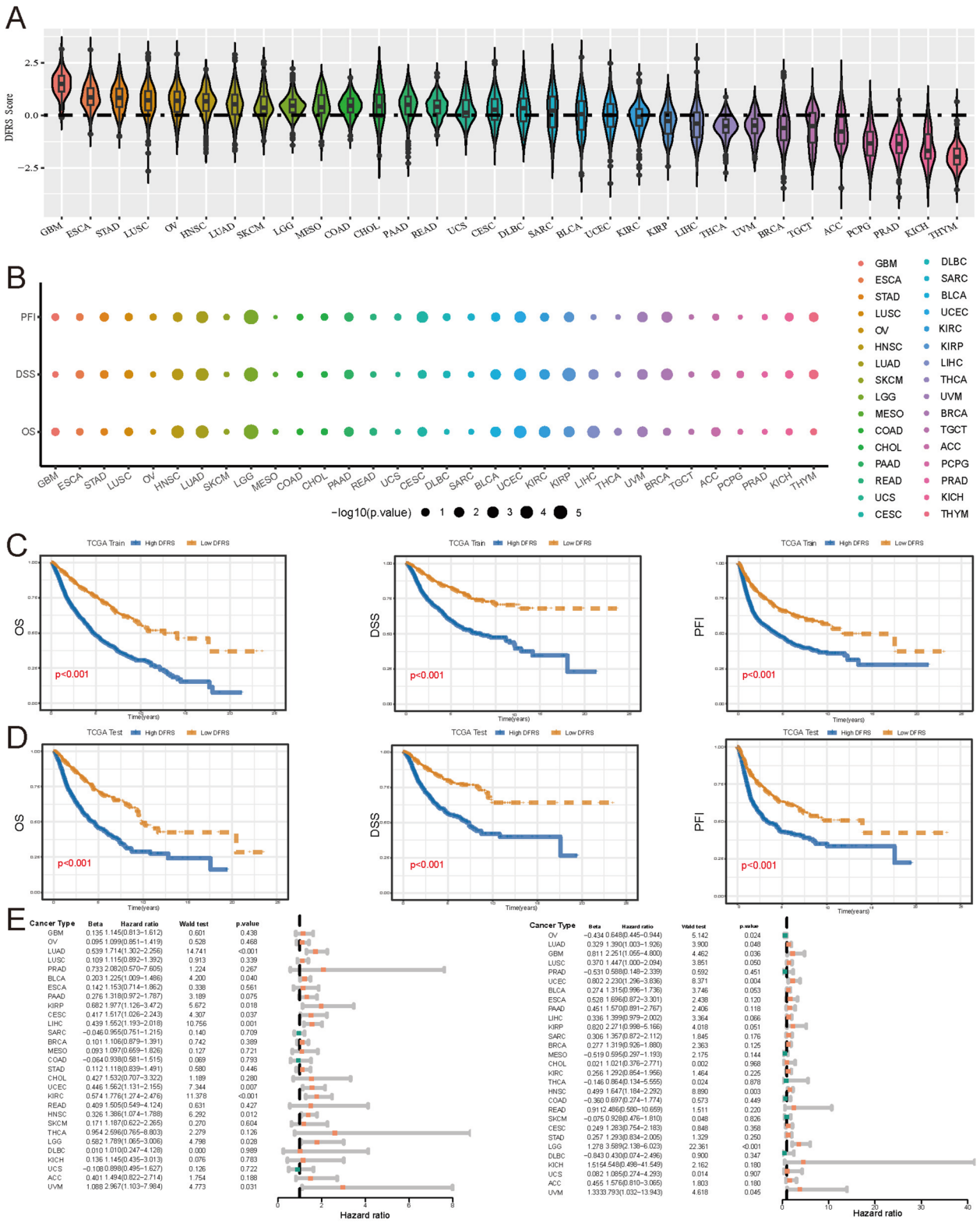

Fig. 3 (See legend on previous page.)

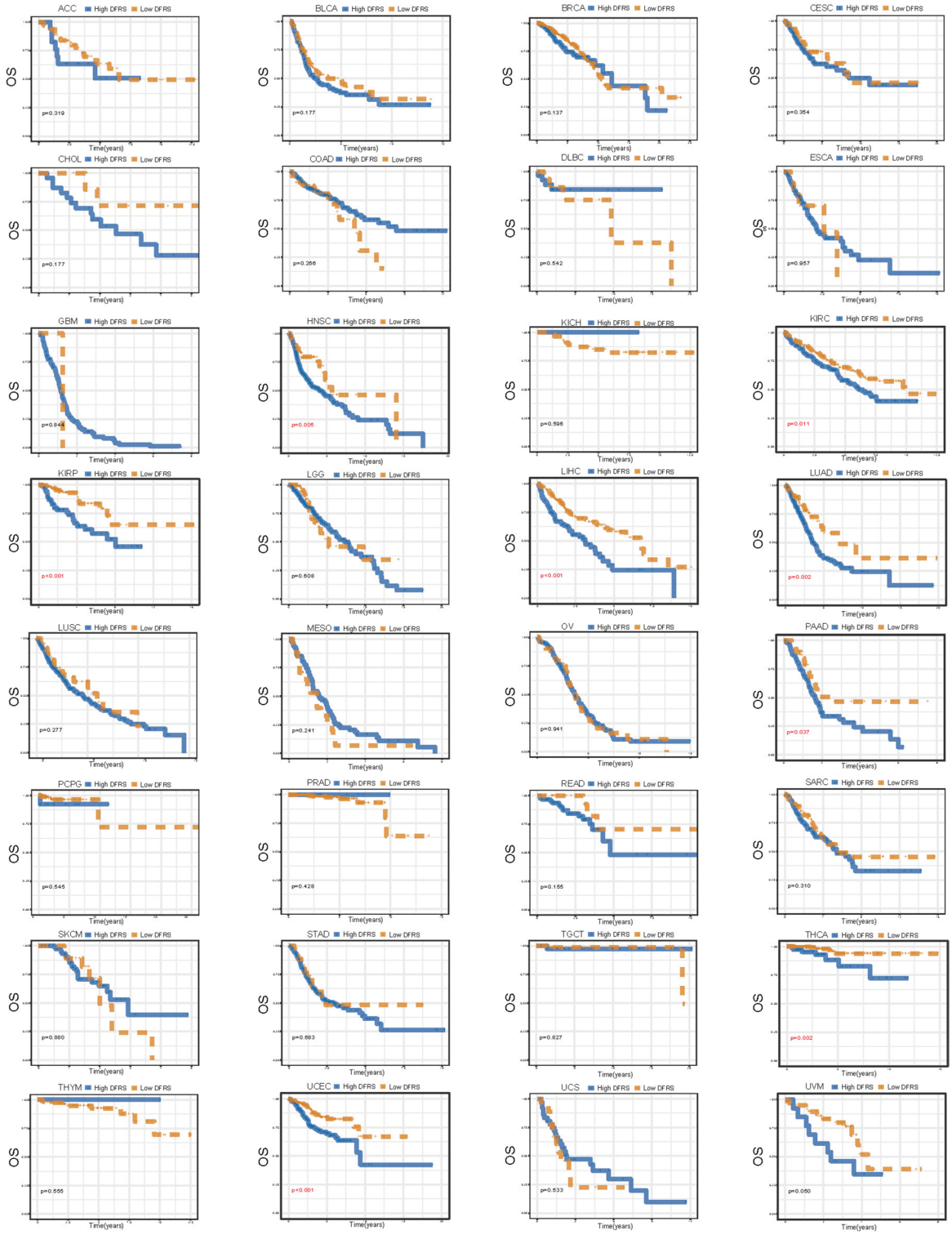

Fig. 4 Kaplan–Meier analysis displaying the connection between the disulfidptosis-related signature (DFRS) score and overall survival of patients in TCGA pan-cancer cohorts. Blue represents high DFRS score, and yellow represents low DFRS score

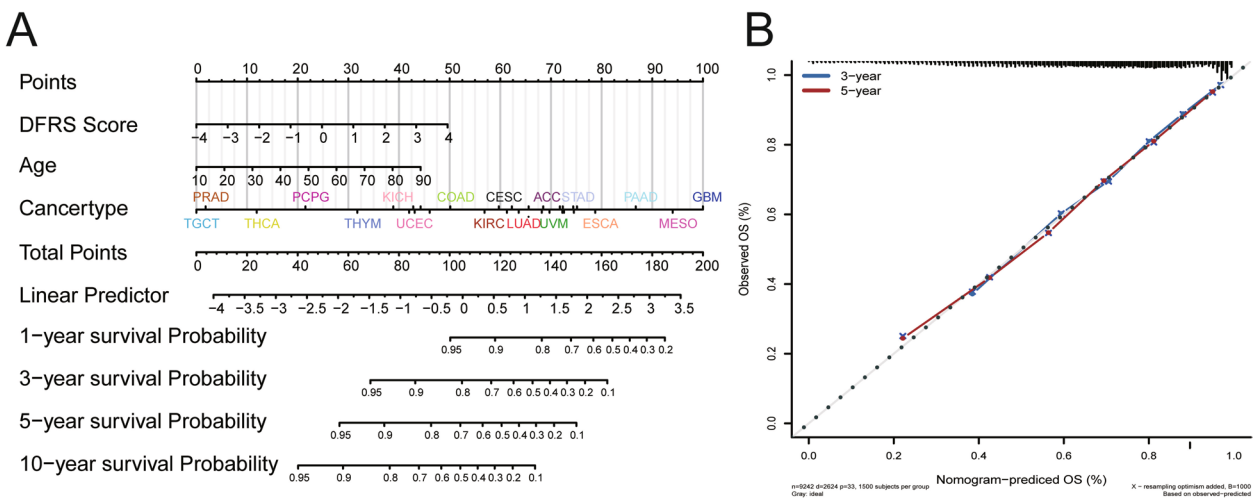

Fig. 5 Evaluating the accuracy of nomogram characteristics in forecasting pan-cancer outcomes. **A** The nomogram integrates various prognostic variables which may include age, disulfidptosis-related signature (DFRS) score, and cancer types. Each factor is represented on a separate line with points assigned based on its prognostic weight. The total points accumulated from all factors correlate with the predicted survival at specific time points, providing a personalized survival prediction. **B** The model's calibration to validate the alignment between predicted and actual survival outcomes. The x-axis represents the predicted survival probabilities, while the y-axis denotes the observed survival probabilities. A 45-degree line indicates perfect prediction accuracy. Points or a line fit to the data show how well the nomogram's predictions match the actual outcomes

metrics. Notably, in 13 of the 32 cancer types analyzed, including BLCA, BRCA, and PAAD, there were substantial positive correlations with the immune score. The DFRS score also showed a positive correlation with the stromal score and an inverse relationship with tumor purity (Fig. 7A). Furthermore, we performed a Spearman correlation analysis between the DFRS score and 75 immune-associated genes [24]. The findings indicated that MHC genes, immunosuppressive genes, chemokines and their receptors predominantly exhibited positive correlations with the DFRS score across various cancers, including ACC, BLCA, BRCA, COAD, Kidney chromophobe (KICH), KIRC, KIRP, LGG, LIHC, Mesothelioma (MESO), Ovarian serous cystadenocarcinoma (OV), PAAD, PCPG, PRAD, Rectum adenocarcinoma (READ), Thymoma (THYM), THCA, and UVM. However, Cholangiocarcinoma (CHOL) and Testicular germ cell tumors (TGCT) exhibited negative correlations (Fig. 7B). By employing the CIBERSORT algorithm, we analyzed the composition of 22 immune cell types within tumor samples [25]. The findings highlighted that the infiltration patterns of immune cells were distinct and cancer specific. For example, the level of CD4 + T memory activated cells was correlated positively with the DFRS score in cancers such as BRCA and BLCA, but it was not a universal trend across all cancers. In addition, the level of tumor growth-promoting macrophages (M1-like) had a negative relationship with the DFRS score in BRCA but a positive relationship in ESCA, which implied an immunostimulatory microenvironment in certain cancer types. These findings suggest a notable association between the DFRS score and the immune landscape in a subset of the cancer types studied, highlighting the potential interplay in specific contexts.

(See figure on next page.)

Fig. 6 The relationship between the disulfidptosis-related signature (DFRS) score and malignant features of the tumor. **A** DFRS z-score and EMT z-score Correlation between the DFRS z-score and angiogenesis z-score across cancers. The x-axis represents the angiogenesis z-score, while the y-axis denotes the DFRS z-score. **B** Correlation between the DFRS z-score and epithelial to mesenchymal transition (EMT) z-score across cancers. The x-axis is the EMT z-score, and the y-axis represents the DFRS z-score. **C** Correlation between the DFRS score and cell cycle distribution across cancers. The x-axis represents the cell cycle z-score, while the y-axis denotes the DFRS z-score. **D** Correlation of the DFRS score and EMT phenotype of 32 cancer types. The x-axis is the EMT z-score, and the y-axis represents the DFRS z-score **E** Enrichment analysis of 50 HALLMARK pathways between tumor samples with high versus low DFRS scores across cancers. Red represents positive correlation, blue represents negative correlation, and the size of the bubble indicates the statistical significance of the association. The x-axis represents 50 HALLMARK pathways, and the y-axis represents the corresponding 32 cancer types

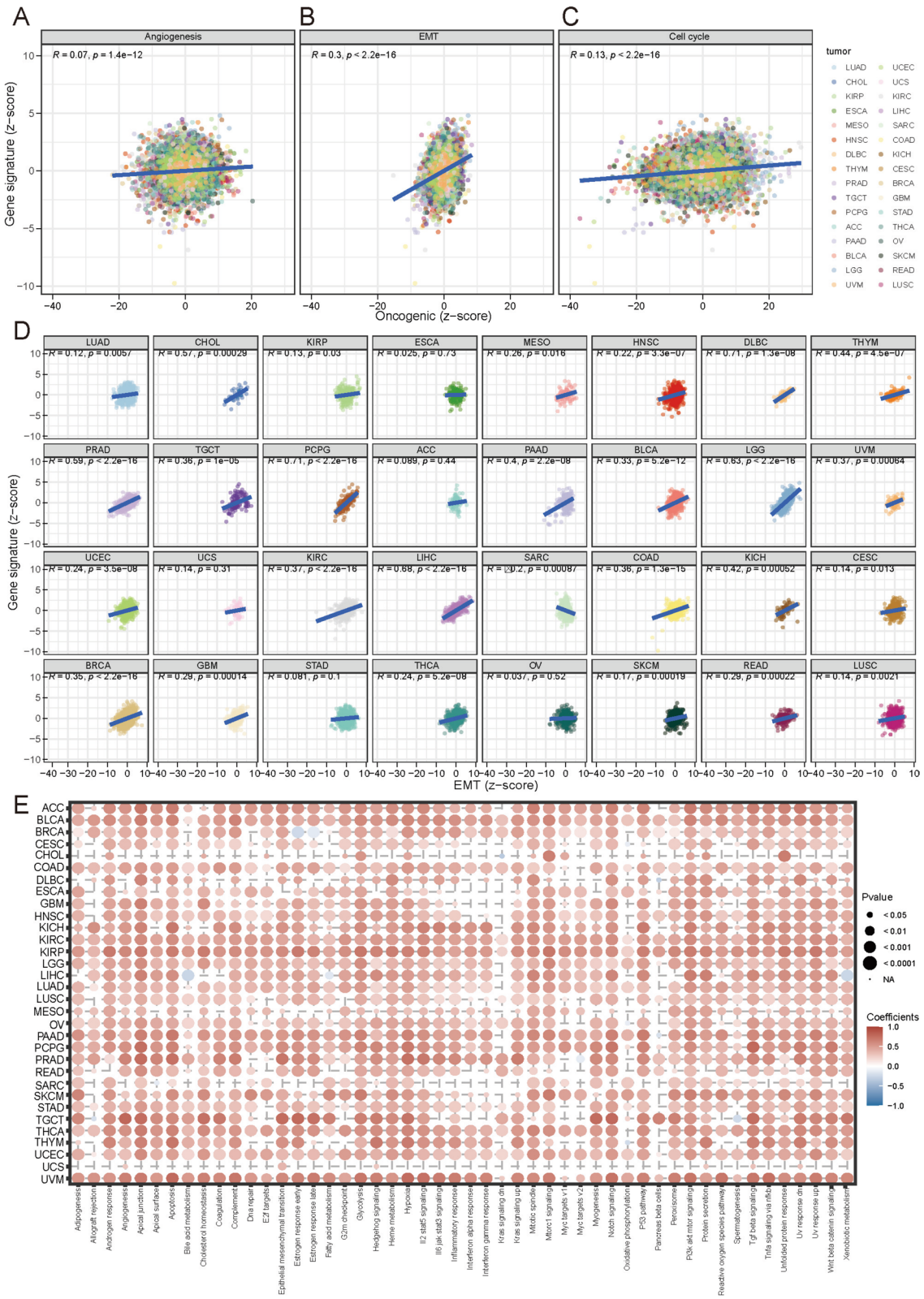

Fig. 6 (See legend on previous page.)

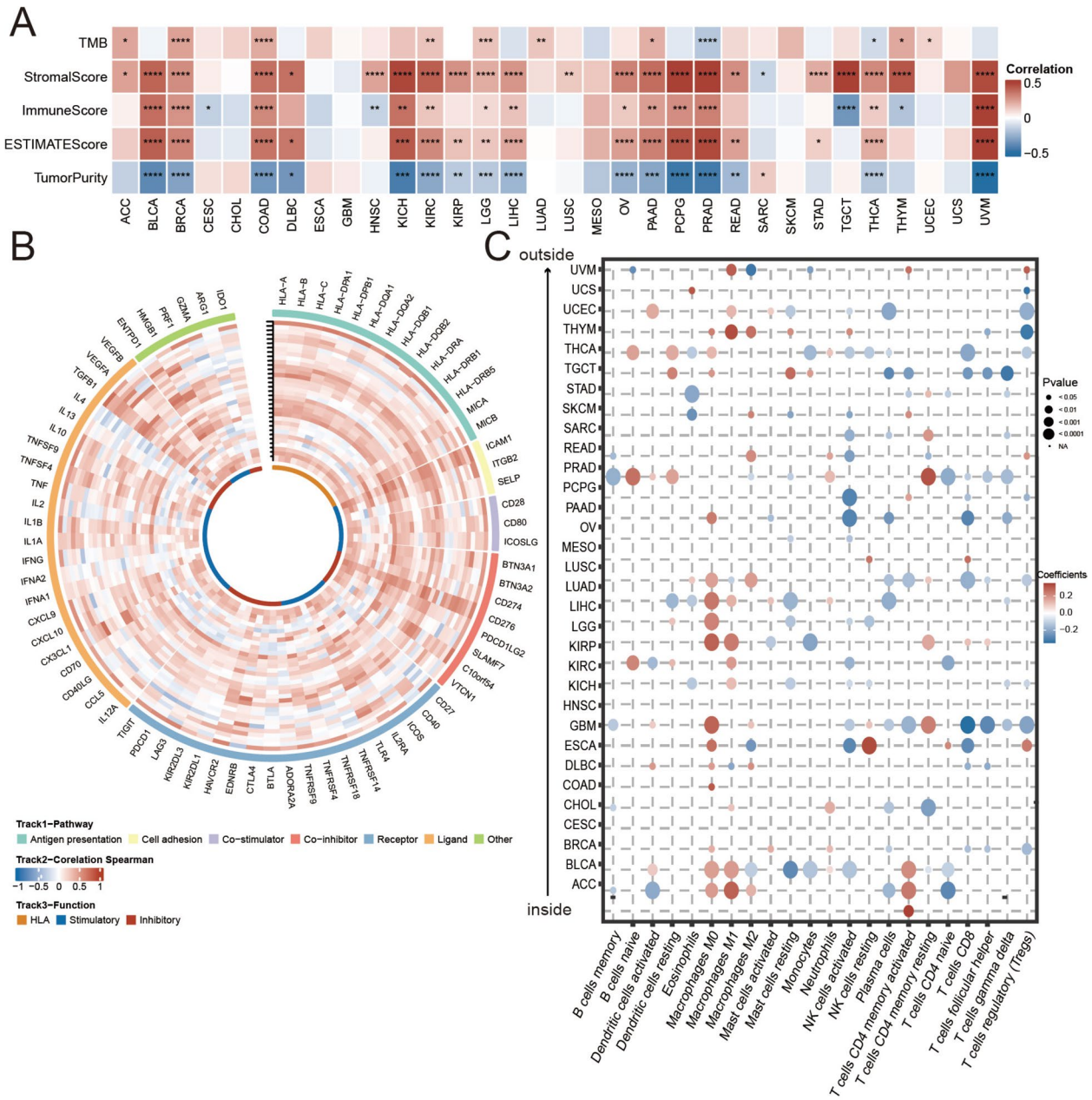

Fig. 7 Correlations between the disulfidptosis-related signature (DFRS) score and immune features. **A** The association between the DFRS score and various metrics, including the immune score, stromal score, ESTIMATE score, tumor purity, and tumor mutational burden (TMB). Red represents positive correlation, blue represents negative correlation. *$p < 0.05$, **$p < 0.01$, ***$p < 0.001$, ****$p < 0.0001$. **B** Circos plot illustrating the ties between the DFRS score and the expression patterns of immune-related genes in diverse cancers. The plot is structured with multiple layers representing different aspects of gene expression correlation. From the innermost to the outer layer, the plot visually encodes the strength of correlation between the DFRS score and various immune genes. Red indicates positive correlations, while blue denotes negative correlations. The vertical reference line, highlighted by a black arrow, marks the delineation of distinct cancer types, each detailed by the y-axis of plot C. **C** A heatmap that details the link between the DFRS score and the levels of infiltrating immune cells across cancers. Each row of the heatmap represents a different type of immune cell, while each column corresponds to a different cancer type. The color intensity within the heatmap indicates the strength of the correlation between the DFRS score and the abundance of each immune cell type. Red represents positive correlation, blue represents negative correlation, and the size of the bubble indicates the statistical significance of the association

Correlation between DFRS Score and immunotherapy response

Immune checkpoint therapy has advanced significantly with the introduction of PD-1/PD-L1 targeting immunotherapies [26, 27]. Exploring the link between the DFRS score and the effectiveness of PD-1/PD-L1 immunotherapies, we assessed the correlation of the DFRS score with tumor mutational burden (TMB). Our analysis showed that the DFRS score was positively correlated with TMB across nine cancer types, including BRCA and BLCA (Fig. 7A). The results suggested that certain cancer types might exhibit heightened sensitivity to immunotherapy in patients with elevated DFRS scores. This hypothesis was further supported by analysis in various immunotherapy datasets, where a high DFRS score generally correlated with better immunotherapy outcomes (Fig. 8A-D). Additionally, analysis of the independent GSE103668 dataset revealed that higher DFRS scores were associated with favorable responses to therapy in triple-negative breast cancer (Fig. 8E). Notably, in both clinical in-house cohorts, patients with higher DFRS scores exhibited better responses to immunotherapy (Fig. 8F-G). In summary, these insights highlighted the potential for the DFRS score to serve as a biomarker for immunotherapy responsiveness.

Drug sensitivity analysis

Investigating the clinical implications of disulfidptosis, we analyzed co-expression between the core genes in the DFRS and 141 clinically actionable genes (CAGs) targeted in therapies across various cancers. These CAGs included 121 genes identified for targeted therapy and 20 genes for immunotherapy in multiple cancers [18, 19]. Our analysis revealed that all 121 CAGs for targeted therapy and the DFRS core genes exhibited significant co-expression associations, with notable variations across different cancers, as shown in Fig. 9A. The number of CAGs associated with the DFRS core genes varied, ranging from 108 in UCS to 121 in UVM (Fig. 9B). The number of pairs of co-expressed genes between the DFRS core genes and CAGs ranged from 522 in UCS to 1477 in KIRC (Fig. 9C). For example, ACTB was positively associated with 20 immunotherapy-targeted genes (Fig. 9D). This suggests that ACTB might influence the efficacy of

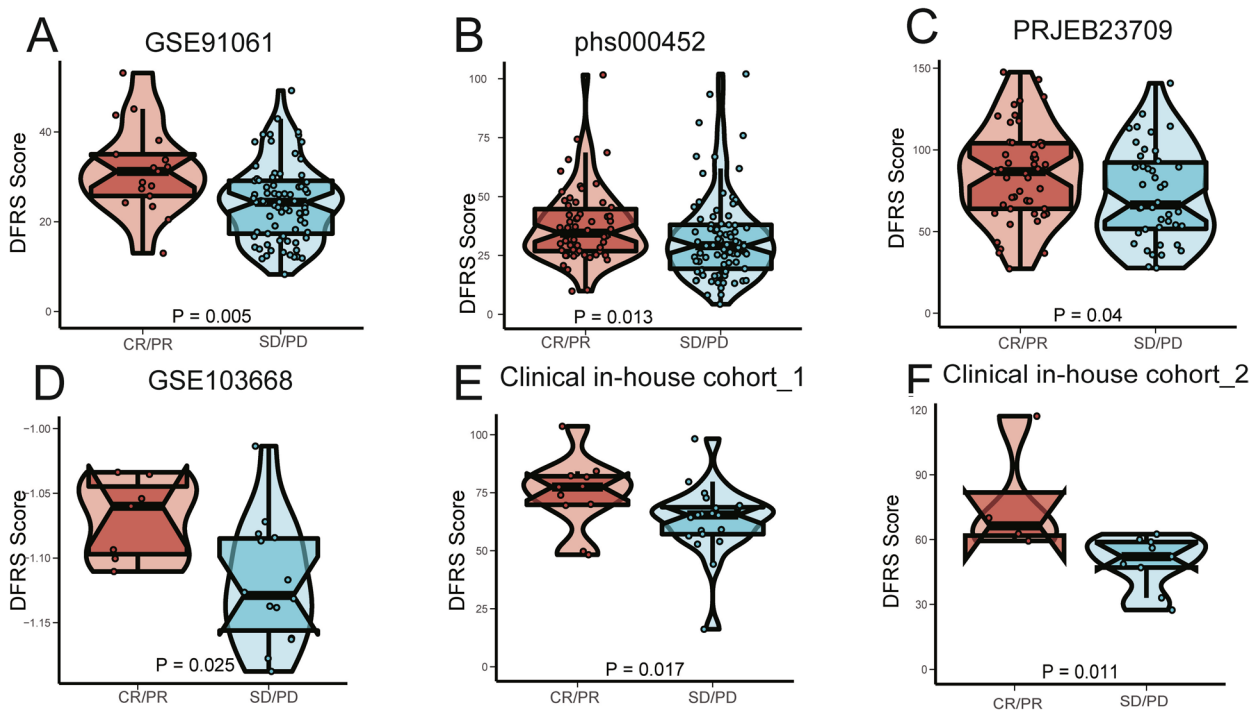

Fig. 8 Analyzing the predictive value of the DFRS score in relation to immunotherapy response. **A**-**C** Violin plots illustrating the DFRS scores in patients with different responses to immunotherapy across four datasets: GSE91061, phs000452, and PRJEB23709. The y-axis indicates the DFRS score, while the x-axis categorizes the patients based on their response status: Complete Response (CR), Partial Response (PR), Stable Disease (SD), and Progressive Disease (PD). **D** Violin plot illustrating the DFRS scores in patient groups based on their responses to treatments from the GSE103668 dataset. The y-axis indicates the DFRS score, while the x-axis categorizes the patients based on their response status (CR, PR, SD, PD). **E**–**F** Violin plots illustrating the DFRS scores in patients with different responses to immunotherapy in two clinical in-house cohorts. The y-axis indicates the DFRS score, while the x-axis categorizes the patients based on their response status: Complete Response (CR), Partial Response (PR), Stable Disease (SD), and Progressive Disease (PD)

cancer immunotherapy. These observations indicate that disulfidptosis modulates drug responses by interacting with CAGs.

To deepen our understanding of the link between disulfidptosis and drug sensitivity, we employed the AUC to evaluate drug responsiveness. The findings showed a remarkable correlation between the DFRS score and sensitivity to 84 distinct drugs. Of these, 19 exhibited a negative correlation, while 65 showed a positive correlation with the DFRS score. To discern the influence of individual the DFRS core genes on drug sensitivity, we examined the relationships between sensitivity to 84 drugs and the expression of the DFRS core genes, identifying 521 significantly correlated DRG-CAG pairs (Fig. 9E). Notably, MYL6 and FLNB were each associated with the AUC values of 76 drugs each. These correlations were used to further categorize the DFRS core genes into two groups. One group comprised genes such as CD2 AP, MYL6, and FLNB. These genes exhibited a positive correlation with the AUCs of BRAF and MEK inhibitors, such as trametinib, selumetinib, refametinib, dabrafenib, and PLX −4720. The other group included genes such as ACTN4 and FLNA, which were negatively associated with the AUC values of BRAF and MEK inhibitors. In conclusion, our findings indicate that both the DFRS score and DRG expression have significant correlations with sensitivity to multiple drugs.

Functional validation of core genes in DFRS for LUAD

To explore the potential value and biological role of high-risk genes (HR > 1) from our model, we focused on NCKAP1 and ACTN4 in lung adenocarcinoma (LUAD). RT-qPCR analysis across A549, PC-9, and BEAS-2B cell lines revealed elevated expression of both NCKAP1 (Fig. 10A) and ACTN4 (Fig. 10B) in LUAD cells compared to normal BEAS-2B controls. Gene-specific silencing was achieved using two independent siRNAs for each target: si-NCKAP1-1/2 and si-ACTN4-1/2. The effective suppression of NCKAP1 and ACTN4 was confirmed by RT-qPCR, as depicted in Fig. 10C-D. This knockdown resulted in a decreased colony formation capability in the A549 cell line, demonstrated in Fig. 10E-F. Moreover, transwell assays revealed that silencing NCKAP1 and ACTN4 impaired the migratory capabilities of A549 cells, as evidenced in Fig. 10G-H. These results collectively suggest that NCKAP1 and ACTN4, as high-risk genes, play a critical role in promoting cell proliferation and migration in LUAD, positioning them as promising therapeutic targets for the treatment of LUAD.

Discussion

Cancer's complexity is accentuated by numerous factors such as altered intracellular metabolism, immune evasion, cell cycle anomalies, and persistent inflammation [28]. The identification of disulfidptosis and its associated mechanisms unveils promising avenues for targeting this novel form of cell death. At the molecular level, disulfidptosis is closely intertwined with various cellular processes and intersects with key cancer-related signaling pathways. For instance, the PI3 K-AKT-mTOR pathway, which is often dysregulated in cancers, may impact the intracellular redox environment, a crucial factor in disulfidptosis. In certain cancer types, the over-activation of this pathway may disrupt cysteine metabolism, a critical element of disulfidptosis, potentially enhancing or inhibiting the process[29]. Furthermore, disulfidptosis does not operate in isolation but interacts with other cell death mechanisms. In certain cancers, the coexistence and interaction between disulfidptosis, apoptosis, necroptosis, and ferroptosis dictate the fate of tumor cells[30]. Recent studies have begun to unravel the clinical relevance of disulfidptosis in specific cancers. For instance, a 2023 study on colon adenocarcinoma (COAD) identified six disulfidptosis-related lncRNAs (DRLs) that strongly correlated with prognosis and immune escape, highlighting the potential of disulfidptosis-related signatures as prognostic biomarkers [31].

Emerging evidence suggests post-translational modifications, particularly S-palmitoylation, may serve as critical regulators of disulfidptosis. While our multi-omics analysis identified widespread dysregulation of DRGs

(See figure on next page.)

Fig. 9 Drug sensitivity analysis. **A** The heatmap displays the DFRS core genes from the disulfidptosis-related signature (DFRS) and 121 drug-targeted genes. The x-axis represents 121 drug-targeted genes, while the y-axis shows 14 the DFRS core genes. Red represents a positive correlation, while blue represents a negative correlation. **B** The count of clinically actionable genes (CAGs) associated with the DFRS core genes across pan-cancer, with the y-axis representing the number of CAGs. **C** The bar chart displays the number of co-expressed DRG-CAG pairs, with the y-axis representing the number of co-expressed DRG-CAG pairs and the x-axis representing 32 cancer types. Yellow indicates positive correlation, and blue indicates negative correlation. **D** This heatmap illustrates the co-expression relationships between the DFRS core genes and 20 genes used in immunotherapy. The x-axis represents genes used in immunotherapy, while the y-axis shows the DFRS core genes, with the strength of co-expression indicated by color intensities. **E** The heatmap explores the correlation between DRG expression levels and the dose–response curve for drugs. The x-axis represents 14 the DFRS core genes, and the y-axis represents 84 drugs. Red represents a positive correlation, while blue represents a negative correlation

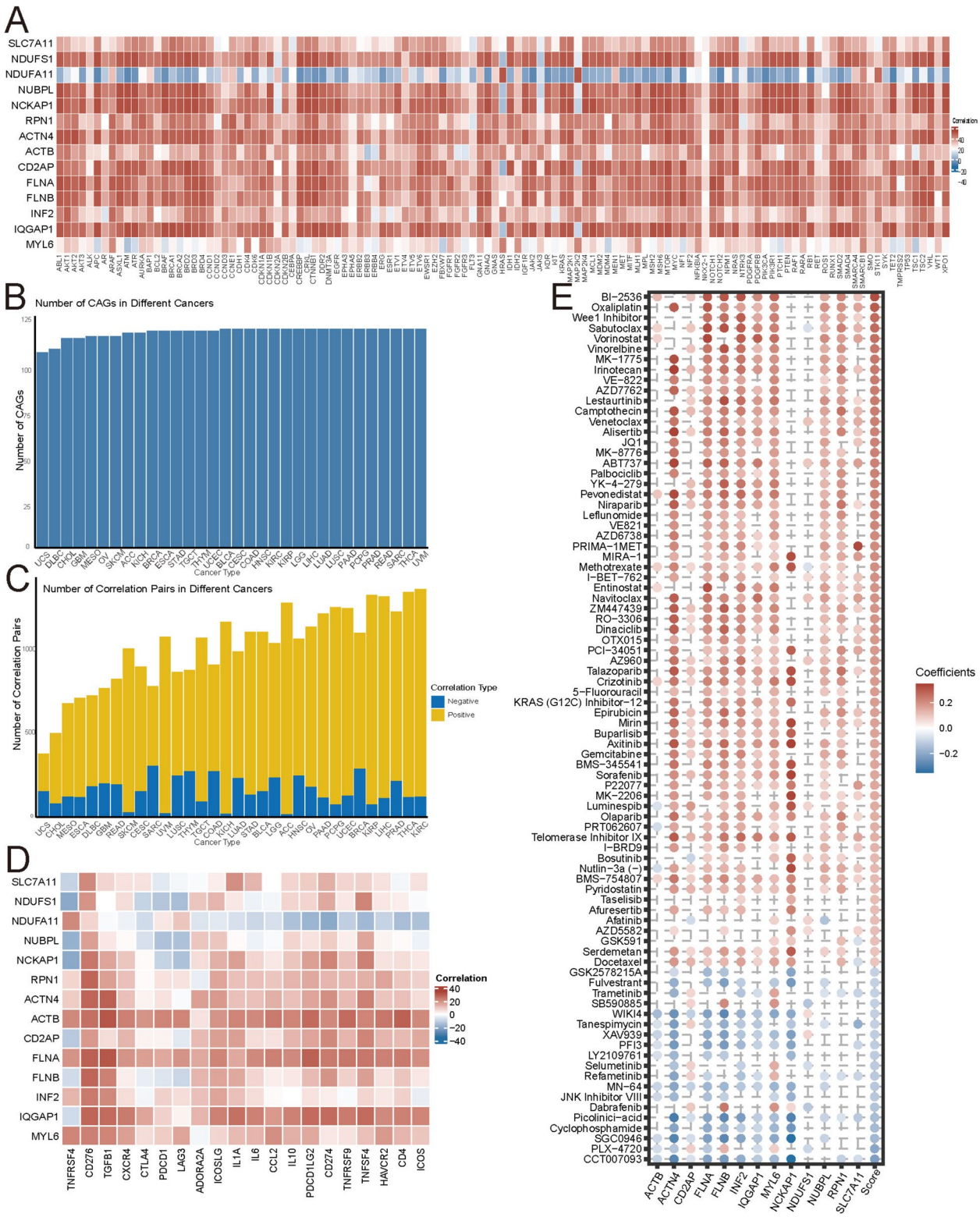

Fig. 9 (See legend on previous page.)

(e.g., SLC7 A11 and GYS1), recent studies reveal that S-palmitoylation dynamically modulates membrane localization and stability of redox-related transporters [32]. Intriguingly, the intersection between palmitoylation and disulfidptosis extends beyond oncology. In diabetic neuropathy, PRDX6 coordinates S-palmitoylation-dependent redox signaling to mitigate oxidative damage—a mechanism that mirrors the NADPH buffering system central to disulfidptosis regulation [33]. Although our study focused on cancer, the shared reliance on cysteine metabolism suggests potential therapeutic cross-talk. For example, PRDX6-mediated palmitoylation in neuronal cells may protect against disulfidptosis-like cascades triggered by glutathione depletion, a phenomenon observed in Parkinson's disease models. This dual role highlights the need for tissue-specific targeting strategies when modulating disulfidptosis-related pathways.

Despite the key role of disulfidptosis in tumors, its exploration across various cancer types remains largely uncharted. No comprehensive studies have delved into the role of disulfidptosis across diverse malignancies. Our study leveraged multi-omics data from various databases to comprehensively assess disulfidptosis-related genetic, epigenetic, and transcriptional alterations in different cancers. We found widespread aberrant expression of DRGs, influenced significantly by copy number alterations and DNA methylation. Employing LASSO and multivariate Cox analyses, we crafted a signature that quantifies disulfidptosis modifications and linked the DFRS score with immune features, survival outcomes, responses to therapies, and drug sensitivities. This connection highlights potential cancer-specific therapeutic opportunities that could improve targeted treatment approaches. Our research builds a foundation for deeper exploration into disulfidptosis in the tumor microenvironment, setting the stage for future biomarker development.

The TME plays a critical role in cancer progression, therapy resistance, and the efficacy of immunotherapy [34]. We examined the relationship between the DFRS score and the TME, finding that the DFRS score positively correlated with immune and stromal scores across multiple cancers, indicating an immune-active TME. This could potentially enhance the effectiveness of immunotherapy in certain cancers. Recent advances emphasize immunotherapy as a transformative treatment, yet variable clinical response rates pose challenges. TMB is recognized as a key indicator for predicting ICI response across a spectrum of cancers [35–37]. Prior research has shown that individuals with elevated TMB levels generally have better response rates and improved outcomes with immunotherapy [38]. Our analysis confirmed a positive relationship between the DFRS score and TMB in nine cancers, including BLCA and BRCA, suggesting that high DFRS scores might predict better responses to ICIs. In addition, prior research has indicated that elevated levels of immune checkpoints correlate with enhanced responsiveness to ICI treatments [39–41]. We found that high DFRS scores were associated with increased expression of immune checkpoints, which could predict improved responses to ICIs. Moreover, in multiple immunotherapy datasets, we identified that patients with a high DFRS score undergoing ICI treatment exhibited superior immunotherapy responses. Therefore, our findings validate the profound association between elevated DFRS scores and the pan-cancer TME and suggest that the DFRS score could be used as a promising biomarker to gauge ICI treatment efficacy in tumor patients. Despite the advances, the detailed molecular mechanisms of disulfidptosis in cancer initiation and progression are still emerging. Our findings linked the DFRS score with key cancer pathways like IL6–JAK–STAT3 and WNT beta-catenin, providing insights into potentially unique tumor dynamics influenced by disulfidptosis. Moreover, we observed that the DFRS core genes were co-expressed with most clinically actionable genes (CAGs), suggesting that disulfidptosis could influence responses to various cancer drugs. This co-expression pattern indicates that targeting these pathways may have broad regulatory effects on tumor behavior, potentially improving therapy outcomes by modulating disulfidptosis.

Our study highlights the potential role of disulfidptosis as a promising target for cancer treatment. This study offers several distinct advantages over prior investigations. First, while earlier research primarily focused on the development and validation of prognostic models for individual cancer types [42–44], our work sought to

(See figure on next page.)

Fig. 10 Role of NCKAP1 in enhancing proliferation and migration in LUAD cells. **A** RT-qPCR validation of NCKAP1 expression across BEAS-2B, A549, and PC9 cell lines. **B** RT-qPCR validation of ACTN4 expression across BEAS-2B, A549, and PC9 cell lines. **C** RT-qPCR analysis confirmed the effective knockdown of NCKAP1 in A549 cells using two siRNAs. **D** RT-qPCR analysis confirmed the effective knockdown of ACTN4 in A549 cells using two siRNAs. **E** ImageJ analysis of colony formation in A549 cells transfected with either control or si-NCKAP1 siRNAs. **F** ImageJ analysis of colony formation in A549 cells transfected with either control or si-ACTN4 siRNAs. **G** Transwell assays comparing the migration of control cells to that of cells with NCKAP1 knockdown. **H** Transwell assays comparing the migration of control cells to that of cells with ACTN4 knockdown. $^{*}p < 0.05$, $^{**}p < 0.01$, $^{***}p < 0.001$.

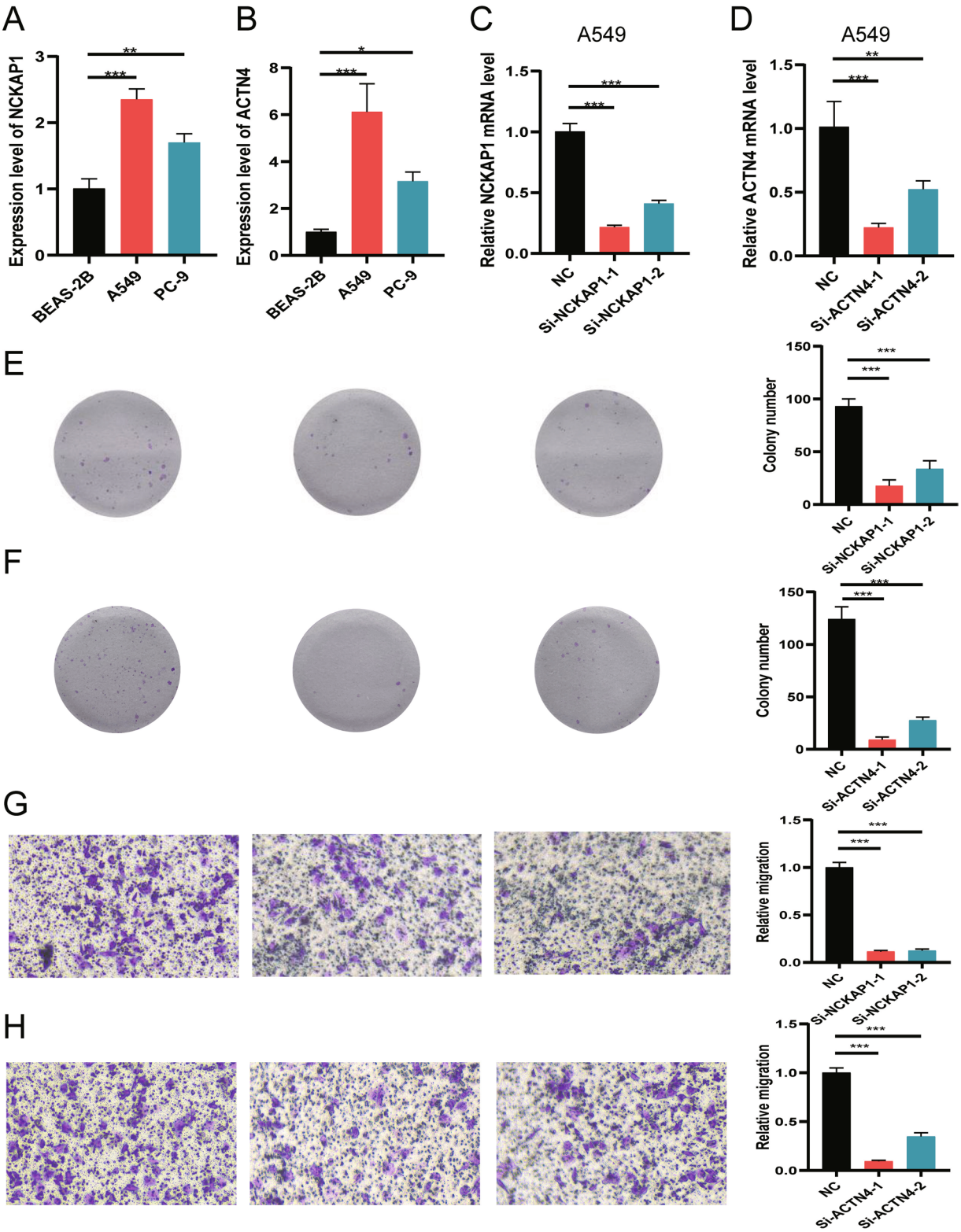

Fig. 10 (See legend on previous page.)

evaluate disulfidptosis levels across cancers, making our signature more broadly applicable. Moreover, our findings provide a comprehensive overview of gene expression patterns, signaling pathways, immunotherapy response, and the clinical value of the DFRS score in cancers. Furthermore, we utilized two in-house cohorts to assess the predictive power of the DFRS score in the context of immunotherapy, demonstrating its practical relevance in real-world settings. This holistic approach has significant implications for both clinical guidelines and clinical practice. However, our study has certain limitations. First, while the DFRS demonstrated moderate prognostic capacity, its predictive accuracy falls short of the thresholds required for direct clinical translation. Additionally, although it has been validated using multiple independent datasets and two in-house clinical cohorts for immunotherapy, further validation in larger, prospectively collected cohorts is essential to improve its discriminative power. Second, while our study identified a potential link between disulfidptosis and cancer-related pathways, such as IL6–JAK–STAT3 and WNT beta-catenin, the precise molecular mechanisms underlying disulfidptosis in cancer progression remain unclear. Future research should focus on experimental validation of these pathways to explore their viability as therapeutic targets. Third, the therapeutic implications of DFRS require further functional investigation. While bioinformatic drug sensitivity predictions hold some value, direct experimental evidence linking disulfidptosis modulation to treatment efficacy remains limited. A systematic CRISPR screening of the DFRS core genes across cancer cell lines, combined with pharmacogenomic profiling, could bridge this knowledge gap. In conclusion, while our findings highlight the potential of disulfidptosis as a pan-cancer biomarker, more extensive studies with diverse datasets, experimental validation, and deeper mechanistic insights are required to fully assess its clinical relevance and therapeutic potential.

Conclusions

This study establishes disulfidptosis as a pan-cancer biomarker system through three key advances. First, we developed the first multi-omics-derived DFRS, integrating 14 core genes, which is capable of predicting the prognosis of certain cancers. Second, the DFRS stratifies tumor immune landscapes, predicting immunotherapy response in melanoma, LUAD, and triple-negative breast cancer. Third, pharmacogenomic profiling revealed druggable targets, and functional validation confirmed the role of ACTN4 and NCKAP1 in LUAD metastasis. These findings transform disulfidptosis from a biochemical phenomenon into a clinical decision framework, providing validated biomarkers and therapeutic combinations for precision oncology.

Supplementary Information

The online version contains supplementary material available at https://doi.org/10.1186/s12885-025-14246-1.

Supplementary Material 1. Fig. S1. Frequency and types of single nucleotide variations (SNVs) in disulfidptosis-related genes (DRGs). (A) Mutation frequency of DRGs in pan-cancer. The redder the color, the higher the mutation frequency. (B) An oncoplot illustrating the mutation distribution of DRGs and detailing various SNV categories in pan-cancer.

Supplementary Material 2. Fig. S2. Kaplan–Meier analysis highlighting the relationship between the disulfidptosis-related signature (DFRS) score and disease-specific survival of patients across TCGA pan-cancer cohorts. Blue represents high DFRS score, and yellow represents low DFRS score.

Supplementary Material 3. Fig S3. Kaplan–Meier analysis highlighting the relationship between the disulfidptosis-related signature (DFRS) score and progression-free interval of patients across TCGA pan-cancer cohorts. Blue represents high DFRS score, and yellow represents low DFRS score.

Supplementary Material 4. Fig. S4. Assessment of the predictive accuracy of the disulfidptosis-related signature (DFRS) in the TCGA training and testing sets using receiver operating characteristic (ROC) curve analysis.

Supplementary Material 5. Fig S5. Prognostic performance of the disulfidptosis-related signature (DFRS) score in external cohorts. Blue represents high DFRS score, and yellow represents low DFRS score.

Supplementary Material 6.

Supplementary Material 7.

Supplementary Material 8.

Supplementary Material 9.

Supplementary Material 10.

Authors' contributions

Shengshan Xu and Zhuming Lu conceptualized and designed the study. Zizhou Chen performed experimental validation and provided clinical in-house cohorts. Shengshan Xu, Zizhou Chen, Xiguang Chen, Hongyu Chu, Xufeng Huang, Chunyu Chen, Hejie Liu, and Yuting Qu performed the data analyses and prepared the figures and tables. Shengshan Xu and Zhuming Lu wrote and revised the manuscript. All authors contributed to the article and approved the submitted version.

Funding

This work was supported by the Medical Science Foundation of Jiangmen Central Hospital (J202401).

Data availability

The datasets analyzed during the current study are available in the GEO, TCGA, METABRIC, ICGC, and CGGA databases (https://www.ncbi.nlm.nih.gov/geo/; https://www.cancer.gov; http://www.cbioportal.org; https://dcc.icgc.org/; http://www.cgga.org.cn). Moreover, the raw data reported in this paper have been deposited in the Genome Sequence Archive in National Genomics Data Center, China National Center for Bioinformation/Beijing Institute of Genomics, Chinese Academy of Sciences (GSA-Human: HRA011082) that are accessible at https://ngdc.cncb.ac.cn/gsa-human.

Declarations

Ethics approval and consent to participate

This study was performed in line with the principles of the Declaration of Helsinki. The studies involving human participants were reviewed and approved by The Clinical Research Ethics Committee of Jiangmen Central Hospital (Approval number: 2023–115). The patients/participants provided their written informed consent to participate in this study.

Consent for publication

Not applicable.

Competing interests
The authors declare no competing interests.

Received: 10 September 2024 Accepted: 29 April 2025
Published online: 01 July 2025

References

1. Siegel RL, Miller KD, Wagle NS, Jemal A: Cancer statistics, 2023. CA: a cancer journal for clinicians 2023, 73(1):17–48.
2. Xu S, Zheng Y, Ye M, Shen T, Zhang D, Li Z, Lu Z. Comprehensive pan-cancer analysis reveals EPHB2 is a novel predictive biomarker for prognosis and immunotherapy response. BMC Cancer. 2024;24(1):1064.
3. Hogg PJ. Biological regulation through protein disulfide bond cleavage. Redox report : communications in free radical research. 2002;7(2):71–7.
4. Wang Y, Jiang Y, Wei D, Singh P, Yu Y, Lee T, Zhang L, Mandl HK, Piotrowski-Daspit AS, Chen X, et al. Nanoparticle-mediated convection-enhanced delivery of a DNA intercalator to gliomas circumvents temozolomide resistance. Nature biomedical engineering. 2021;5(9):1048–58.
5. Chen C, Shen M, Liao H, Guo Q, Fu H, Yu J, Duan Y. A paclitaxel and microRNA-124 coloaded stepped cleavable nanosystem against triple negative breast cancer. Journal of nanobiotechnology. 2021;19(1):55.
6. Koppula P, Zhuang L, Gan B. Cystine transporter SLC7A11/xCT in cancer: ferroptosis, nutrient dependency, and cancer therapy. Protein Cell. 2021;12(8):599–620.
7. Liu X, Nie L, Zhang Y, Yan Y, Wang C, Colic M, Olszewski K, Horbath A, Chen X, Lei G, et al. Actin cytoskeleton vulnerability to disulfide stress mediates disulfidptosis. Nat Cell Biol. 2023;25(3):404–14.
8. Wang J, Chen J, Fan K, Wang M, Gao M, Ren Y, Wu S, He Q, Tu K, Xu Q, et al. Inhibition of Endoplasmic Reticulum Stress Cooperates with SLC7A11 to Promote Disulfidptosis and Suppress Tumor Growth upon Glucose Limitation. Adv Sci (Weinh). 2025;12(7): e2408789.
9. Miller CG, Holmgren A, Arnér ESJ, Schmidt EE. NADPH-dependent and -independent disulfide reductase systems. Free Radic Biol Med. 2018;127:248–61.
10. Gide TN, Quek C, Menzies AM, Tasker AT, Shang P, Holst J, Madore J, Lim SY, Velickovic R, Wongchenko M, et al. Distinct Immune Cell Populations Define Response to Anti-PD-1 Monotherapy and Anti-PD-1/Anti-CTLA-4 Combined Therapy. Cancer Cell. 2019;35(2):238-255.e236.
11. Ritchie ME, Phipson B, Wu D, Hu Y, Law CW, Shi W, Smyth GK. limma powers differential expression analyses for RNA-sequencing and microarray studies. Nucleic Acids Res. 2015;43(7): e47.
12. Lee E, Chuang HY, Kim JW, Ideker T, Lee D. Inferring pathway activity toward precise disease classification. PLoS Comput Biol. 2008;4(11): e1000217.
13. Şenbabaoğlu Y, Gejman RS, Winer AG, Liu M, Van Allen EM, de Velasco G, Miao D, Ostrovnaya I, Drill E, Luna A, et al. Tumor immune microenvironment characterization in clear cell renal cell carcinoma identifies prognostic and immunotherapeutically relevant messenger RNA signatures. Genome Biol. 2016;17(1):231.
14. Tirosh I, Izar B, Prakadan SM, Wadsworth MH 2nd, Treacy D, Trombetta JJ, Rotem A, Rodman C, Lian C, Murphy G, et al. Dissecting the multicellular ecosystem of metastatic melanoma by single-cell RNA-seq. Science (New York, NY). 2016;352(6282):189–96.
15. Hänzelmann S, Castelo R, Guinney J. GSVA: gene set variation analysis for microarray and RNA-seq data. BMC Bioinformatics. 2013;14:7.
16. Subramanian A, Tamayo P, Mootha VK, Mukherjee S, Ebert BL, Gillette MA, Paulovich A, Pomeroy SL, Golub TR, Lander ES, et al. Gene set enrichment analysis: a knowledge-based approach for interpreting genome-wide expression profiles. Proc Natl Acad Sci USA. 2005;102(43):15545–50.
17. Newman AM, Liu CL, Green MR, Gentles AJ, Feng W, Xu Y, Hoang CD, Diehn M, Alizadeh AA. Robust enumeration of cell subsets from tissue expression profiles. Nat Methods. 2015;12(5):453–7.
18. Mak MP, Tong P, Diao L, Cardnell RJ, Gibbons DL, William WN, Skoulidis F, Parra ER, Rodriguez-Canales J, Wistuba II, et al. A Patient-Derived, Pan-Cancer EMT Signature Identifies Global Molecular Alterations and Immune Target Enrichment Following Epithelial-to-Mesenchymal Transition. Clinical cancer research : an official journal of the American Association for Cancer Research. 2016;22(3):609–20.
19. Van Allen EM, Wagle N, Stojanov P, Perrin DL, Cibulskis K, Marlow S, Jane-Valbuena J, Friedrich DC, Kryukov G, Carter SL, et al. Whole-exome sequencing and clinical interpretation of formalin-fixed, paraffin-embedded tumor samples to guide precision cancer medicine. Nat Med. 2014;20(6):682–8.
20. Yang W, Soares J, Greninger P, Edelman EJ, Lightfoot H, Forbes S, Bindal N, Beare D, Smith JA, Thompson IR et al: Genomics of Drug Sensitivity in Cancer (GDSC): a resource for therapeutic biomarker discovery in cancer cells. Nucleic acids research 2013, 41(Database issue):D955–961.
21. Shen H, Laird PW. Interplay between the cancer genome and epigenome. Cell. 2013;153(1):38–55.
22. Salmon H, Remark R, Gnjatic S, Merad M. Host tissue determinants of tumour immunity. Nat Rev Cancer. 2019;19(4):215–27.
23. Yoshihara K, Shahmoradgoli M, Martínez E, Vegesna R, Kim H, Torres-Garcia W, Treviño V, Shen H, Laird PW, Levine DA, et al. Inferring tumour purity and stromal and immune cell admixture from expression data. Nat Commun. 2013;4:2612.
24. Thorsson V, Gibbs DL, Brown SD, Wolf D, Bortone DS, Ou Yang TH, Porta-Pardo E, Gao GF, Plaisier CL, Eddy JA, et al. The Immune Landscape of Cancer. Immunity. 2018;48(4):812-830.e814.
25. Chen B, Khodadoust MS, Liu CL, Newman AM, Alizadeh AA. Profiling Tumor Infiltrating Immune Cells with CIBERSORT. Methods in molecular biology (Clifton, NJ). 2018;1711:243–59.
26. Ribas A, Wolchok JD. Cancer immunotherapy using checkpoint blockade. Science (New York, NY). 2018;359(6382):1350–5.
27. Xia L, Liu Y, Wang Y. PD-1/PD-L1 Blockade Therapy in Advanced Non-Small-Cell Lung Cancer: Current Status and Future Directions. Oncologist. 2019;24(Suppl 1):S31-s41.
28. Alexander SPH, Mathie A, Peters JA, Veale EL, Striessnig J, Kelly E, Armstrong JF, Faccenda E, Harding SD, Pawson AJ et al: THE CONCISE GUIDE TO PHARMACOLOGY 2019/20: Ion channels. British journal of pharmacology 2019, 176 Suppl 1(Suppl 1):S142-s228.
29. Gu Q, An Y, Xu M, Huang X, Chen X, Li X, Shan H, Zhang M: Disulfidptosis, A Novel Cell Death Pathway: Molecular Landscape and Therapeutic Implications. Aging Dis 2024, Online ahead of print. https://doi.org/10.14336/AD.2024.0083.
30. Li Y, Zhang H, Yang F, Zhu D, Chen S, Wang Z, Wei Z, Yang Z, Jia J, Zhang Y, et al. Mechanisms and therapeutic potential of disulphidptosis in cancer. Cell Prolif. 2025;58(1): e13752.
31. Chen P, Yu J, Luo Q, Li J, Wang W. Construction of disulfidptosis-related lncRNA signature for predicting the prognosis and immune escape in colon adenocarcinoma. BMC Gastroenterol. 2023;23(1):382.
32. Zhang Y, Li F, Fu K, Liu X, Lien IC, Li H. Potential Role of S-Palmitoylation in Cancer Stem Cells of Lung Adenocarcinoma. Front Cell Dev Biol. 2021;9:734897.
33. Cao Y, Wang W, Zhan X, Zhang Y. PRDX6: A protein bridging S-palmitoylation and diabetic neuropathy. Front Endocrinol (Lausanne). 2022;13:992875.
34. Binnewies M, Roberts EW, Kersten K, Chan V, Fearon DF, Merad M, Coussens LM, Gabrilovich DI, Ostrand-Rosenberg S, Hedrick CC, et al. Understanding the tumor immune microenvironment (TIME) for effective therapy. Nat Med. 2018;24(5):541–50.
35. Phillips D, Matusiak M, Gutierrez BR, Bhate SS, Barlow GL, Jiang S, Demeter J, Smythe KS, Pierce RH, Fling SP, et al. Immune cell topography predicts response to PD-1 blockade in cutaneous T cell lymphoma. Nat Commun. 2021;12(1):6726.
36. Scheiner B, Pomej K, Kirstein MM, Hucke F, Finkelmeier F, Waidmann O, Himmelsbach V, Schulze K, von Felden J, Fründt TW, et al. Prognosis of patients with hepatocellular carcinoma treated with immunotherapy - development and validation of the CRAFITY score. J Hepatol. 2022;76(2):353–63.
37. Yu G, Pang Y, Merchant M, Kesserwan C, Gangalapudi V, Abdelmaksoud A, Ranjan A, Kim O, Wei JS, Chou HC, et al. Tumor Mutation Burden, Expressed Neoantigens and the Immune Microenvironment in Diffuse Gliomas. Cancers. 2021;13(23):6092.
38. Li R, Han D, Shi J, Han Y, Tan P, Zhang R, Li J. Choosing tumor mutational burden wisely for immunotherapy: A hard road to explore. Biochim Biophys Acta. 2020;1874(2): 188420.
39. Xu-Monette ZY, Zhou J, Young KH. PD-1 expression and clinical PD-1 blockade in B-cell lymphomas. Blood. 2018;131(1):68–83.

40. Qin S, Xu L, Yi M, Yu S, Wu K, Luo S. Novel immune checkpoint targets: moving beyond PD-1 and CTLA-4. Mol Cancer. 2019;18(1):155.
41. Chauvin JM, Zarour HM. TIGIT in cancer immunotherapy. J Immunother Cancer. 2020;8(2): e000957.
42. Feng Z, Zhao Q, Ding Y, Xu Y, Sun X, Chen Q, Zhang Y, Miao J, Zhu J. Identification a unique disulfidptosis classification regarding prognosis and immune landscapes in thyroid carcinoma and providing therapeutic strategies. J Cancer Res Clin Oncol. 2023;149(13):11157–70.
43. Liu L, Liu J, Lyu Q, Huang J, Chen Y, Feng C, Liu Y, Chen F, Wang Z. Disulfidptosis-associated LncRNAs index predicts prognosis and chemotherapy drugs sensitivity in cervical cancer. Sci Rep. 2023;13(1):12470.
44. Li J, Yang C, Zheng Y. A novel disulfidptosis and glycolysis related risk score signature for prediction of prognosis and ICI therapeutic responsiveness in colorectal cancer. Sci Rep. 2023;13(1):13344.

Publisher's Note